

Chapter 8: Nested Nonlinear Multiscale Frameworks for the Analysis of Thick-Section Composite Materials and Structures

Rami Haj-Ali

Georgia Institute of Technology, Atlanta, GA 30332-0355, USA
rami.haj-ali@ce.gatech.edu

8.1 Introduction

This chapter presents nonlinear and time-dependent multiscale frameworks for the analysis of thick-section and multilayered composite materials and structures. Nested and hierarchical three-dimensional (3D) micromechanical models are formulated within the nonlinear analysis framework. The constitutive framework is composed of nonlinear material models for the matrix behavior, micromodels for the unidirectional lamina, and a sublaminar model for a repeating ply-stacking sequence. A unified development of a class of constant deformation cell (CDC) micromodels is presented to generate the effective nonlinear response of a unidirectional lamina from the response of its matrix and fiber constituents (subcells). Two structural modeling approaches for nonlinear analysis of laminated composites are proposed using 3D and shell nonlinear finite element (FE) analysis. The first, for the analysis of multilayered and thick-section composites, uses the 3D sublaminar model coupled with 3D FE structural models. The sublaminar represents the nonlinear effective continuum response of a through-thickness repeating stacking sequence at the FE material points (Gaussian integration points). The CDC micromodels can be employed for the different layers within the sublaminar model. The second structural approach is used for the analysis of thin-section laminated composite plates and shells in the form of a ply-by-ply. In this

case, the micromodels are used to represent the effective response of each layer. New stress-update solution algorithms are developed for the micromodels and the sublaminated model; they are well suited for nonlinear displacement-based FE. Different applications are presented and comparisons are made with reported experimental results. The proposed micromodels are shown to be very capable of predicting the response of different composite materials and structural systems, such as multilayered laminated composites and thick-section pultruded composites. The numerical stress-update algorithms are shown to be well behaved and robust. Applications presented using the proposed frameworks indicate their suitability as practical, general material, and structural analysis tools.

Unlike traditional structural materials, such as metals, composite materials add a new and exciting dimension to the engineering design process. Their effective material properties and strengths can be controlled based on the choice of the matrix and fiber materials, volume fractions, and multiaxial reinforcements, along with several other material, geometry and manufacturing parameters. Proper selection of these parameters in the design process can lead to an optimal structural design, such as a structure with minimum weight and a maximum resistance to the applied forces.

Composite materials are widely used in high-performance structures where high stiffness and strength combined with low weight are required. Today, many structural components are made from composite materials, especially in the aviation industry. However, it is still rare to find a complete structure that is fully made of composite materials. This indicates that the analysis, design, and manufacturing of composite structures have not yet fully reached a satisfactory level of reliability. Therefore, there is still a need to improve and introduce new analysis and design approaches that can predict the nonlinear and damage behavior of composites.

Recently, the use of composite technology in civil and infrastructure applications, such as bridges and construction joints, has been advocated. However, there are two major obstacles standing in the way: the relatively high manufacturing cost and the lack of sufficient predictive models to provide information on the behavior of such structures over their lifespan. Nevertheless, in some cases, the relatively high cost of using composite materials can be justified. For example, the use of composite materials in bridges can eliminate the need to reinforce the concrete with steel bars that are subject to corrosion, thereby prolonging the lifespan of the bridge

which can compensate for the higher cost of the composite structure. In addition, it is evident that advances in mass manufacturing of composite materials will drive costs down. This provides additional incentive to continue the research on the behavior of composite structures in civil and infrastructure applications.

The tremendous advances in computer technology that have taken place over the last two decades have made possible the development of computational tools that routinely employ nonlinear analysis for practical engineering applications. The use of nonlinear stress–strain relations, such as those provided by plasticity and other inelastic models, is now considered a standard engineering practice. However, nonlinear structural modeling approaches that use 3D analysis are not widespread for laminated composites. This is due to many factors. Laminated composites are often considered as brittle materials without accounting for their nonlinear behavior. Therefore, elastic structural analysis and design are often considered sufficient. Furthermore, many laminated structures are thin shell structures that can be idealized using plane-stress constitutive models. However, nonlinear 3D structural analyses may be needed to produce reliable structural designs. Even in the case of thin shell structures, a realistic nonlinear 3D constitutive model is needed to depict accurately the structural response in the presence of edge effects and structural discontinuities. These discontinuities, such as crack tips, holes, and cutouts, usually have a significant impact on the response of the structure, because damage will typically initiate at and propagate from these locations. Therefore, it is important to develop nonlinear and three-dimensional material models to properly simulate the structural behavior with local nonlinear and damage responses.

Macroscale nonlinear constitutive models can be formulated directly at the lamina level. On the other hand, micromechanical models of nonlinear lamina behavior, which explicitly recognize the fiber and matrix constituents, are appealing because they can provide more detailed response information than macromechanical models. They are also potentially simpler to formulate because they operate at a more fundamental level than macromechanical models. However, the direct use of micromechanical models in practical nonlinear analysis of laminated structures requires compromise between accuracy and computational effort.

This chapter reviews multiscale material and structural frameworks that allow the application of several micromechanical models while

performing nonlinear structural analysis. A class of simple 3D micro-models that strike a reasonable balance between accuracy and simplicity is reviewed. These nonlinear micromechanical models, e.g., for a unidirectional lamina, are incorporated into a hierarchical framework that is suitable for FE analysis. The structural analysis includes both nonlinear material and geometric effects. The hierarchical nature of this framework allows the use of several alternative combinations of material and structural modeling approaches. The nonlinear material behavior can arise from different sources: matrix nonlinear constitutive behavior, micro-failure effects, e.g., matrix microcracking, fiber–matrix debonding, and fiber failure, e.g., fiber buckling. Several examples of structural analyses are presented and compared with experimental results where possible.

8.2 Multiscale Analysis of Laminated Composite Structures

A general 3D multiscale framework is proposed for the nonlinear analysis of laminated composite structures. Figure 8.1 illustrates the proposed analysis framework for multilayered structures using 3D or shell-based structural FE models. In the case of a 3D FE structural model, a sublaminar model is formulated to represent the nonlinear effective continuum response at each material point (Gaussian point) [24, 25, 33, 34]. The sublaminar model is used to generate a 3D through-thickness effective response of a representative stacking sequence.

In the case of shell elements, Fig. 8.1 illustrates that each layer is explicitly modeled with one or more integration points under plane-stress condition; and the sublaminar model is reduced to the classical lamination theory in this case. Constant transverse shear, cross-sectional stiffness is assumed for the shell elements. This assumption is valid where the transverse stresses in the different layers are very small compared to the in-plane stresses. The 3D micromechanical models provide for the effective nonlinear constitutive behavior for each Gaussian point. The shell element's effective through-thickness response is generated at select integration points on its reference surface by integrating the effective micromechanical response over all Gaussian points, as shown in Fig. 8.1.

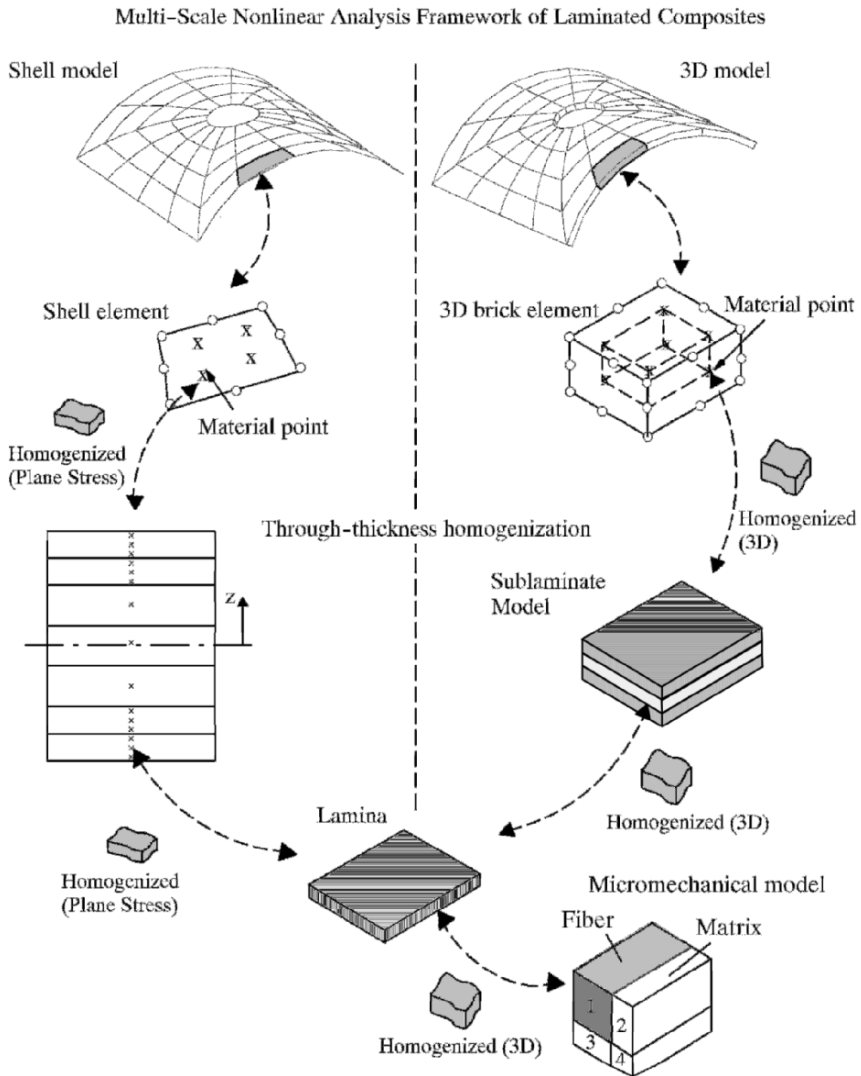


Fig. 8.1. A multiscale micromechanical–structural framework for nonlinear and viscoelastic analysis of laminated composite structures (adapted from [23])

8.3 A Simplified Class of Micromechanical Constitutive Models

A unified approach for defining and characterizing a simple and phenomenological class of nonlinear micromechanical models for fiber composites is presented in this section. A unified development of a class of CDC micromodels, or unit cell (UC), is presented to generate the effective nonlinear continuum response from the average response of its matrix and fiber constituents (subcells). The main advantage of these simple multicell models lies in their ability to generate the full 3D effective stress–strain response of fiber composites in a form that is suitable for integration into finite element structural analysis. The first part of this section sets out some general definitions and relations that are valid for all the micromodels in this class. Specific micromodels are presented in the later part of this section and through this chapter.

The objective of the CDC models is to generate the nonlinear effective stress–strain relations by employing a simple geometrical representation of the unit cell geometry and satisfy traction and displacement continuity between the cells in an average sense. Few assumptions are made at this stage regarding the fiber and matrix constitutive relations; specific material nonlinear constitutive behavior is characterized only at the more fundamental subcell level. The resulting unit cell effective stress–strain relations can be viewed, from a global/structural perspective, as a material model with microstructural constraints.

It is assumed that, for a given heterogeneous periodic medium, it is possible to define a basic unit cell that represents the medium's geometrical and material characteristics. Each unit cell is divided into a number of subcells. Within each subcell, the spatial variation of the displacement field is assumed such that the stresses and deformations are *spatially* uniform in each subcell. Traction continuity at an interface between subcells can, therefore, be satisfied only in an average sense. Some general definitions and linearized formulations are established that are applicable to any CDC micromodel.

The volume average stress over the unit cell is defined as

$$\bar{\sigma}_{ij} = \frac{1}{V} \int_V \sigma_{ij}(x) dV = \frac{1}{V} \sum_{\alpha=1}^N \int_{V_{(\alpha)}} \sigma_{ij}^{(\alpha)}(x^{(\alpha)}) dV_{(\alpha)} = \frac{1}{V} \sum_{\alpha=1}^N V_{(\alpha)} \sigma_{ij}^{(\alpha)}, \quad (8.1)$$

where N is the number of subcells and V is the unit cell volume. A similar definition applies for volume average strain $\bar{\varepsilon}_{ij}^{(\alpha)}$. The superscript α denotes the subcell number. An overbar denotes a unit cell average quantity. The variables x and $x^{(\alpha)}$ are the unit cell global and the subcell local coordinates, respectively. Stress and strain are uniform within each subcell by definition. Therefore, using matrix notation

$$\bar{\sigma} = \frac{1}{V} \sum_{\alpha=1}^N V_{(\alpha)} \sigma^{(\alpha)}, \quad \bar{\varepsilon} = \frac{1}{V} \sum_{\alpha=1}^N V_{(\alpha)} \varepsilon^{(\alpha)}, \quad V = \sum_{\alpha=1}^N V_{(\alpha)}, \quad (8.2)$$

where the stresses and strains are now written as vectors.

Next, a strain-concentration or strain-interaction fourth rank tensor B is defined for each subcell, which relates the subcell strain increment to the unit cell average strain increment

$$d\varepsilon_{ij}^{(\alpha)} = B_{ijkl}^{(\alpha)} d\bar{\varepsilon}_{kl}. \quad (8.3)$$

It is important to emphasize that the interaction matrices are unknown at this stage; they will be determined later in this section by solution of the unit cell governing equations. It can be easily shown that a subcell strain-interaction matrix is usually a function of the tangent stiffness and the relative volumes of all subcells.

Using the incremental form of (8.2) with (8.3), expressed in matrix notation, the average strain increment of the unit cell is:

$$d\bar{\varepsilon} = \frac{1}{V} \sum_{\alpha=1}^N V_{(\alpha)} d\varepsilon^{(\alpha)} = \frac{1}{V} \sum_{\alpha=1}^N V_{(\alpha)} B^{(\alpha)} d\bar{\varepsilon}. \quad (8.4)$$

Since (8.4) must hold for an arbitrary average strain increment $d\bar{\varepsilon}$, the following relations must be satisfied

$$\frac{1}{V} \sum_{\alpha=1}^N V_{(\alpha)} B^{(\alpha)} = I \quad \text{and} \quad \sum_{\alpha=1}^N V_{(\alpha)} (B^{(\alpha)} - I) = 0, \quad (8.5)$$

where I is a unit matrix. The second relation in (8.5) follows from the first relation due to the volume sum relation expressed in (8.2). The matrix representation of the strain-concentration tensor is not symmetric. Next, the incremental stress-strain relations are used to express the stress increment in each of the subcells

$$d\sigma^{(\alpha)} = C^{(\alpha)} d\varepsilon^{(\alpha)} = C^{(\alpha)} B^{(\alpha)} d\bar{\varepsilon}, \quad (8.6)$$

where $C^{(\alpha)}$ is the current tangent stiffness matrix of the subcell. The incremental form of the average stress can be expressed, using (8.6), as:

$$d\bar{\sigma} = \frac{1}{V} \sum_{\alpha=1}^N V_{(\alpha)} \sigma^{(\alpha)} = \frac{1}{V} \sum_{\alpha=1}^N V_{(\alpha)} C^{(\alpha)} B^{(\alpha)} d\bar{\varepsilon}. \quad (8.7)$$

Equation (8.7) can be expressed as

$$d\bar{\sigma} = C^* d\bar{\varepsilon}, \quad (8.8)$$

where C^* is the unit cell effective tangent stiffness matrix defined by:

$$C^* = \frac{1}{V} \sum_{\alpha=1}^N V_{(\alpha)} C^{(\alpha)} B^{(\alpha)}. \quad (8.9)$$

An alternative for deriving the stiffness matrix is to use the second variation of the strain energy density. This is demonstrated by the following relations:

$$d\bar{\varepsilon}^T d\bar{\sigma} = \frac{1}{V} \sum_{\alpha=1}^N V_{(\alpha)} d\varepsilon^{(\alpha)T} d\sigma^{(\alpha)} = d\bar{\varepsilon}^T \left[\frac{1}{V} \sum_{\alpha=1}^N V_{(\alpha)} B^{(\alpha)T} C^{(\alpha)} B^{(\alpha)} \right] d\bar{\varepsilon}. \quad (8.10)$$

Substituting (8.8) into the left-hand side of (8.10), the unit cell stiffness matrix is expressed as:

$$C^* = \frac{1}{V} \sum_{\alpha=1}^N V_{(\alpha)} B^{(\alpha)\top} C^{(\alpha)} B^{(\alpha)}. \quad (8.11)$$

The two expressions for the effective stiffness matrix in (8.9) and (8.11) must be identical. It can be easily verified that, since the strain-concentration matrices $B^{(\alpha)}$ satisfy the relations in (8.5), the two stiffness expressions are, in fact, identical. Equation (8.11) shows that the unit cell stiffness matrix C^* is symmetric provided that the stiffness matrix of each of the subcells $C^{(\alpha)}$ is also symmetric. However, it is interesting to note that this property is not explicitly apparent by a first examination of the expression in (8.9).

Up to this stage, the properties of the strain-interaction matrices and the expression for the unit cell effective stiffness matrix have been dealt with. The only assumption that was made is that the subcells have uniform stress and strain. Therefore, these linearized relations are general for any CDC micromodel. To derive the strain-interaction matrices for a unit cell, the traction and displacement continuity conditions must be imposed, and stress-strain relations must be invoked. The fact that the strains and stresses are uniform in every subcell makes it possible to express the traction and displacement continuity conditions directly in terms of the average stress and strain vectors. The term *strain compatibility* will be used here to describe the relations between the strains in the subcells which satisfy displacement continuity in an average fashion. The combined set of equations that describe the strain compatibility and the traction continuity equations (micromechanical constraints) can ultimately be written in a general incremental form as:

$$dR_{\sigma} = \bar{C}_i (d\sigma^{(\alpha)}, d\varepsilon^{(\alpha)}, d\bar{\varepsilon}, V_{(\alpha)}, \alpha = 1, 2, \dots, N) = 0, \quad i = 1, \dots, n. \quad (8.12)$$

Equation (8.12) is used to generate the strain-interaction matrices for the subcells. The incremental form of the stress-strain relations in the subcells (8.6) is used to express the constraints in terms of the incremental strains

$$dR_{\varepsilon} = E_j (C^{(\alpha)}, d\varepsilon^{(\alpha)}, d\bar{\varepsilon}, V_{(\alpha)}, \alpha = 1, 2, \dots, N) = 0, \quad j = 1, \dots, m. \quad (8.13)$$

$$\begin{bmatrix} B^{(1)} \\ B^{(2)} \\ \vdots \\ B^{(N)} \end{bmatrix} = \begin{bmatrix} A^{-1} \end{bmatrix} \begin{bmatrix} D \end{bmatrix}. \quad (8.16)$$

The stress analysis of a micromechanical unit cell becomes a straightforward procedure as a result of this formulation. Given an average strain increment and the history of deformations in the subcells, the strain-interaction matrices are formed using (8.16). The strain increments are subsequently formed in each of the subcells followed by the corresponding stress increments. This procedure is a linearized incremental stress analysis and will be referred to as the *trial state*. If only this linearized trial analysis is used, two types of error will result at each trial increment and will accumulate during the analysis. It is important to mention, however, that the strain compatibility and traction continuity constraints are exactly satisfied by the trial state which is composed of tangential approximations. The first error occurs in the strain increments because the strain-interaction matrices are derived using the tangent stiffness matrices of the subcells at the beginning of the increment. The second error occurs as a result of using the tangent stiffness to compute the stress increment. Therefore, a *correction scheme* must be used to accurately account for the nonlinear constitutive (with or without damage) material behavior (prediction) and its associated error in the incremental micromechanical equations. New general correction algorithms have been derived for different CDC type micromechanical models with nonlinear and time-dependent behavior, e.g., [16, 18, 20, 22–24].

A four-cell micromodel is formulated next using the previous tangential and stress-update formulations. This model was originally formulated using the method of cells (MOCs), e.g., [2–6]. Aboudi's MOC or GMOC has been shown to be well suited for highly nonlinear matrix response, such as that exhibited by metal matrix composites. However, integration of the MOC formulation in general 3D analysis of composite structures can be tremendously enhanced using the proposed numerical formulation because of the large computational effort that is needed to be performed at each material point (Gaussian point) of the FEA. Therefore, it is important to employ the above efficient stress-update and stress-correction formulations for this model that are suitable for nonlinear

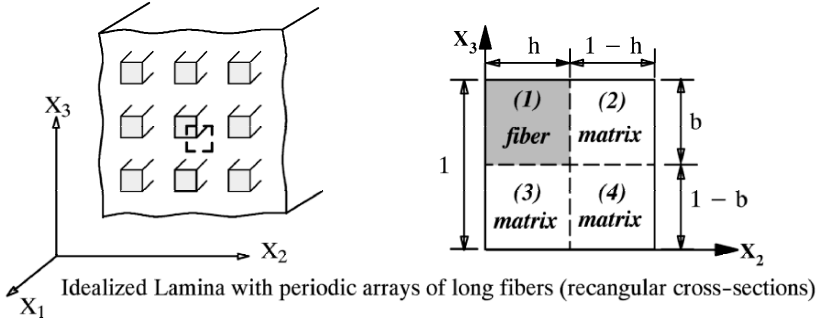


Fig. 8.2. Unit cell micromodel for unidirectional reinforced composites

structural analysis. Next, an incremental formulation of the four-cell model is presented in terms of the average stresses and strains in the subcells. New stress-update and stress-correction algorithms are developed which significantly reduce the computational effort that is needed. The new algorithms are formulated given a constant average strain rate for each time step, which makes them suitable for integration with FE constitutive framework.

The micromechanical model is shown in Fig. 8.2. The unidirectional composite, which consists of long fibers arranged unidirectionally in the matrix system, is idealized as doubly periodic array of fibers with rectangular cross-section. A quarter UC that consists of four subcells is modeled due to symmetry. The first subcell is a fiber constituent, while subcells 2–4 represent the matrix constituents. The long fibers are aligned in the x_1 -direction. The other cross-section directions are referred to as the *transverse directions*. The x_3 -direction is called the out-of-plane axis or lamina thickness direction. The total volume of the UC is taken to be equal to one. The volumes of the four subcells are:

$$V_1 = bh, \quad V_2 = h(1-b), \quad V_3 = b(1-h), \quad V_4 = (1-h)(1-b). \quad (8.17)$$

The notations used for the stress and strain vectors are:

$$\begin{aligned} d\sigma_k^{(\alpha)} &= \{d\sigma_{11}, d\sigma_{22}, d\sigma_{33}, d\tau_{12}, d\tau_{13}, d\tau_{23}\}, & \alpha &= 1, \dots, 4, \\ d\varepsilon_k^{(\alpha)} &= \{d\varepsilon_{11}, d\varepsilon_{22}, d\varepsilon_{33}, d\gamma_{12}, d\gamma_{13}, d\gamma_{23}\}, & k &= 1, \dots, 6. \end{aligned} \quad (8.18)$$

The 3D nonlinear constitutive integration for the fiber and matrix constituents is performed separately for each subcell. The fiber is linear elastic and transversely isotropic, while the matrix medium is viscoelastic.

The homogenization of the micromodel should satisfy displacement and traction continuity. Perfect bond is assumed along the interfaces of the subcells. In the fiber direction, the four subcells satisfy the same strain continuity relation. The axial average stress definition is used as a second independent relation to relate the effective axial stress to the stresses in the subcells. The following equations summarize the relations in the axial mode

$$\begin{aligned} d\varepsilon_1^{(1)} &= d\varepsilon_1^{(2)} = d\varepsilon_1^{(3)} = d\varepsilon_1^{(4)} = d\bar{\varepsilon}_1, \\ V_1 d\sigma_1^{(1)} + V_2 d\sigma_1^{(2)} + V_3 d\sigma_1^{(3)} + V_4 d\sigma_1^{(4)} &= d\bar{\sigma}_1, \end{aligned} \tag{8.19}$$

where overbar denotes an overall average quantity over the unit cell.

Along the interfaces between the subcells with normal in the x_2 -direction, the in-plane stress components σ_{22} and τ_{12} must satisfy traction continuity conditions. The total strain components ε_{22} and γ_{12} from subcells 1 and 2 and subcells 3 and 4, respectively, should also satisfy strain compatibility conditions. These relations are written in an incremental form as:

$$\begin{aligned} d\sigma_2^{(1)} &= d\sigma_2^{(2)}, \\ d\sigma_2^{(3)} &= d\sigma_2^{(4)}, \\ \frac{V_1}{V_1 + V_2} d\varepsilon_2^{(1)} + \frac{V_2}{V_1 + V_2} d\varepsilon_2^{(2)} &= d\bar{\varepsilon}_2, \\ \frac{V_3}{V_3 + V_4} d\varepsilon_2^{(3)} + \frac{V_4}{V_3 + V_4} d\varepsilon_2^{(4)} &= d\bar{\varepsilon}_2, \end{aligned} \tag{8.20}$$

$$\begin{aligned} d\sigma_4^{(1)} &= d\sigma_4^{(2)}, \\ d\sigma_4^{(3)} &= d\sigma_4^{(4)}, \\ \frac{V_1}{V_1 + V_2} d\varepsilon_4^{(1)} + \frac{V_2}{V_1 + V_2} d\varepsilon_4^{(2)} &= d\bar{\varepsilon}_4, \\ \frac{V_3}{V_3 + V_4} d\varepsilon_4^{(3)} + \frac{V_4}{V_3 + V_4} d\varepsilon_4^{(4)} &= d\bar{\varepsilon}_4. \end{aligned} \tag{8.21}$$

Considering interfaces between subcells with normal in the x_3 -direction, the out-of-plane stress components σ_{33} and τ_{13} must satisfy

traction continuity conditions. The total strain components ε_{33} and γ_{13} from subcells 1 and 3 and subcells 2 and 4, respectively, should also satisfy strain compatibility conditions. These relations are expressed in incremental form as:

$$\begin{aligned} d\sigma_3^{(1)} &= d\sigma_3^{(3)}, \\ d\sigma_3^{(2)} &= d\sigma_3^{(4)}, \\ \frac{V_1}{V_1+V_3} d\varepsilon_3^{(1)} + \frac{V_3}{V_1+V_3} d\varepsilon_3^{(3)} &= d\bar{\varepsilon}_3, \\ \frac{V_2}{V_2+V_4} d\varepsilon_3^{(2)} + \frac{V_4}{V_2+V_4} d\varepsilon_3^{(4)} &= d\bar{\varepsilon}_3, \end{aligned} \quad (8.22)$$

$$\begin{aligned} d\sigma_5^{(1)} &= d\sigma_5^{(3)}, \\ d\sigma_5^{(2)} &= d\sigma_5^{(4)}, \\ \frac{V_1}{V_1+V_3} d\varepsilon_5^{(1)} + \frac{V_3}{V_1+V_3} d\varepsilon_5^{(3)} &= d\bar{\varepsilon}_5, \\ \frac{V_2}{V_2+V_4} d\varepsilon_5^{(2)} + \frac{V_4}{V_2+V_4} d\varepsilon_5^{(4)} &= d\bar{\varepsilon}_5. \end{aligned} \quad (8.23)$$

Finally, both types of interfaces should satisfy transverse shear stress continuity. Therefore, the transverse shear stresses in the four subcells are equal to the effective transverse shear stress. The transverse shear strains from the four subcells in the average strain definition are used to express the relations with the effective transverse shear strain of the UC. The transverse shear relations are summarized as:

$$\begin{aligned} d\sigma_6^{(1)} &= d\sigma_6^{(2)} = d\sigma_6^{(3)} = d\sigma_6^{(4)} = d\bar{\sigma}_6, \\ V_1 d\varepsilon_6^{(1)} + V_2 d\varepsilon_6^{(2)} + V_3 d\varepsilon_6^{(3)} + V_4 d\varepsilon_6^{(4)} &= d\bar{\varepsilon}_6. \end{aligned} \quad (8.24)$$

Equations (8.19)–(8.24) along with the stress–strain relations within each fiber and matrix subcells complete the micromechanical formulation of the unidirectional lamina. These relations are used in incremental (rate) form due to the nonlinear constitutive relations in the matrix subcells. Next, the

strain components in the subcells are grouped into two parts (a) and (b). The first part corresponds to the incremental compatibility equations and the second part is the traction continuity relations (homogeneous equations). The two groups of strain vectors are defined by:

$$\mathbf{d}\boldsymbol{\varepsilon}_a^T = \left\{ \begin{array}{l} \mathbf{d}\boldsymbol{\varepsilon}_1^{(1)}, \mathbf{d}\boldsymbol{\varepsilon}_1^{(2)}, \mathbf{d}\boldsymbol{\varepsilon}_1^{(3)}, \mathbf{d}\boldsymbol{\varepsilon}_1^{(4)}, \mathbf{d}\boldsymbol{\varepsilon}_2^{(1)}, \mathbf{d}\boldsymbol{\varepsilon}_2^{(3)}, \mathbf{d}\boldsymbol{\varepsilon}_4^{(1)}, \\ \mathbf{d}\boldsymbol{\varepsilon}_4^{(3)}, \mathbf{d}\boldsymbol{\varepsilon}_3^{(1)}, \mathbf{d}\boldsymbol{\varepsilon}_3^{(2)}, \mathbf{d}\boldsymbol{\varepsilon}_5^{(1)}, \mathbf{d}\boldsymbol{\varepsilon}_5^{(2)}, \mathbf{d}\boldsymbol{\varepsilon}_6^{(1)} \end{array} \right\}, \quad (8.25)$$

$$\mathbf{d}\boldsymbol{\varepsilon}_b^T = \left\{ \begin{array}{l} \mathbf{d}\boldsymbol{\varepsilon}_2^{(2)}, \mathbf{d}\boldsymbol{\varepsilon}_2^{(4)}, \mathbf{d}\boldsymbol{\varepsilon}_4^{(2)}, \mathbf{d}\boldsymbol{\varepsilon}_4^{(4)}, \mathbf{d}\boldsymbol{\varepsilon}_3^{(3)}, \mathbf{d}\boldsymbol{\varepsilon}_3^{(4)} \\ \mathbf{d}\boldsymbol{\varepsilon}_5^{(3)}, \mathbf{d}\boldsymbol{\varepsilon}_5^{(4)}, \mathbf{d}\boldsymbol{\varepsilon}_6^{(2)}, \mathbf{d}\boldsymbol{\varepsilon}_6^{(3)}, \mathbf{d}\boldsymbol{\varepsilon}_6^{(4)} \end{array} \right\}. \quad (8.26)$$

Equations (8.19)–(8.24) can be expressed in terms of the strain increments in the subcells after substituting the incremental stress–strain relations. The rearrangement of the strain increments allows this set of equations to be transformed into the previous general CDC form presented in (8.15), where $\mathbf{d}R_\sigma$ is the residual form of the stress relations (traction continuity) expressed incrementally in terms of the strains in the subcells. The matrices that appear in (8.15) for this UC micromodel are listed below and can be identified by examining (8.17)–(8.24). The nonzero terms of \bar{A}_{ab} are:

$$\begin{aligned} \bar{A}_{ab}(5,1) &= \bar{A}_{ab}(6,2) = \bar{A}_{ab}(7,3) = \bar{A}_{ab}(8,4) = \bar{A}_{ab}(13,9) = \frac{1-h}{h}, \\ \bar{A}_{ab}(9,5) &= \bar{A}_{ab}(10,6) = \bar{A}_{ab}(11,7) = \bar{A}_{ab}(12,8) = \bar{A}_{ab}(13,10) = \frac{1-b}{b}, \\ \bar{A}_{ab}(13,11) &= \frac{(1-b)(1-h)}{bh}. \end{aligned} \quad (8.27)$$

The nonzero terms of \bar{D}_a are:

$$\begin{aligned}
 \bar{D}_a(1,1) &= \bar{D}_a(2,1) = \bar{D}_a(3,1) = \bar{D}_a(4,1) = 1, \\
 \bar{D}_a(5,2) &= \bar{D}_a(6,2) = \bar{D}_a(7,4) = \bar{D}_a(8,4) = \frac{1}{h}, \\
 \bar{D}_a(9,3) &= \bar{D}_a(10,3) = \bar{D}_a(11,5) = \bar{D}_a(12,5) = \frac{1}{b}, \\
 \bar{D}_a(13,6) &= \frac{1}{bh}.
 \end{aligned}
 \tag{8.28}$$

The terms of \bar{A}_{ba} and \bar{A}_{bb} matrices are listed in (8.29) and (8.30), respectively. Only the inverse of the (11 × 11) submatrix in (8.15) is needed to solve for $d\varepsilon_a$ and $d\varepsilon_b$. The strain-concentration matrices are determined by solving $dR_\sigma = 0$ and $dR_\varepsilon = 0$ equations as previously outlined

$$\bar{A}_{ba} = \begin{bmatrix}
 -C_{12}^{(1)} & C_{12}^{(2)} & 0 & 0 & -C_{22}^{(1)} & 0 & 0 & 0 & -C_{23}^{(1)} & C_{23}^{(2)} & 0 & C_{25}^{(2)} & 0 \\
 0 & 0 & -C_{12}^{(3)} & C_{12}^{(4)} & 0 & -C_{22}^{(3)} & 0 & -C_{24}^{(3)} & 0 & 0 & 0 & 0 & 0 \\
 0 & C_{14}^{(2)} & 0 & 0 & 0 & 0 & -C_{44}^{(1)} & 0 & 0 & C_{34}^{(2)} & 0 & C_{45}^{(2)} & 0 \\
 0 & 0 & -C_{14}^{(3)} & C_{14}^{(4)} & 0 & -C_{24}^{(3)} & 0 & -C_{44}^{(3)} & 0 & 0 & 0 & 0 & 0 \\
 -C_{12}^{(1)} & 0 & C_{13}^{(3)} & 0 & -C_{23}^{(1)} & C_{23}^{(3)} & 0 & C_{34}^{(3)} & -C_{22}^{(1)} & 0 & 0 & 0 & 0 \\
 0 & -C_{13}^{(2)} & 0 & C_{13}^{(4)} & 0 & 0 & 0 & 0 & 0 & -C_{33}^{(2)} & 0 & -C_{35}^{(2)} & 0 \\
 0 & 0 & C_{15}^{(3)} & 0 & 0 & C_{25}^{(3)} & 0 & C_{45}^{(3)} & 0 & 0 & -C_{44}^{(1)} & 0 & 0 \\
 0 & -C_{15}^{(2)} & 0 & C_{15}^{(4)} & 0 & 0 & 0 & 0 & 0 & -C_{35}^{(2)} & 0 & -C_{55}^{(2)} & 0 \\
 0 & C_{16}^{(2)} & 0 & 0 & 0 & 0 & 0 & 0 & 0 & C_{36}^{(2)} & 0 & C_{56}^{(2)} & -C_{66}^{(1)} \\
 0 & 0 & C_{16}^{(3)} & 0 & 0 & C_{26}^{(3)} & 0 & C_{46}^{(3)} & 0 & 0 & 0 & 0 & -C_{66}^{(1)} \\
 0 & -C_{16}^{(2)} & 0 & C_{16}^{(4)} & 0 & 0 & 0 & 0 & 0 & -C_{36}^{(2)} & 0 & -C_{56}^{(2)} & 0
 \end{bmatrix}
 \tag{8.29}$$

$$\bar{\mathbf{A}}_{\text{bb}} = \begin{bmatrix} C_{22}^{(2)} & 0 & C_{24}^{(2)} & 0 & 0 & 0 & 0 & 0 & 0 & C_{26}^{(2)} & 0 & 0 \\ 0 & C_{22}^{(4)} & 0 & C_{24}^{(4)} & -C_{23}^{(3)} & C_{23}^{(4)} & -C_{25}^{(3)} & C_{25}^{(4)} & 0 & -C_{26}^{(3)} & C_{26}^{(4)} \\ C_{24}^{(2)} & 0 & C_{44}^{(2)} & 0 & 0 & 0 & 0 & 0 & 0 & C_{46}^{(2)} & 0 & 0 \\ 0 & C_{24}^{(4)} & 0 & C_{44}^{(4)} & -C_{34}^{(3)} & C_{34}^{(4)} & -C_{45}^{(3)} & C_{45}^{(4)} & 0 & -C_{46}^{(3)} & C_{46}^{(4)} \\ 0 & 0 & 0 & 0 & C_{33}^{(3)} & 0 & C_{35}^{(3)} & 0 & 0 & C_{36}^{(3)} & 0 \\ -C_{23}^{(2)} & C_{23}^{(4)} & -C_{34}^{(2)} & C_{34}^{(4)} & 0 & C_{33}^{(4)} & 0 & C_{35}^{(4)} & -C_{36}^{(2)} & 0 & C_{36}^{(4)} \\ 0 & 0 & 0 & 0 & C_{35}^{(3)} & 0 & C_{55}^{(3)} & 0 & 0 & C_{56}^{(3)} & 0 \\ -C_{25}^{(2)} & C_{25}^{(4)} & -C_{45}^{(2)} & C_{45}^{(4)} & 0 & C_{35}^{(4)} & 0 & C_{55}^{(4)} & -C_{56}^{(2)} & 0 & C_{56}^{(4)} \\ C_{26}^{(2)} & 0 & C_{46}^{(2)} & 0 & 0 & 0 & 0 & 0 & 0 & C_{66}^{(2)} & 0 & 0 \\ 0 & 0 & 0 & 0 & C_{36}^{(3)} & 0 & C_{56}^{(3)} & 0 & 0 & C_{66}^{(3)} & 0 \\ -C_{26}^{(2)} & C_{26}^{(4)} & -C_{46}^{(2)} & C_{46}^{(4)} & 0 & C_{36}^{(4)} & 0 & C_{56}^{(4)} & -C_{66}^{(2)} & 0 & C_{66}^{(4)} \end{bmatrix} \quad (8.30)$$

The micromechanical relations are exact only in the case of linear stress–strain relations in the fiber and matrix subcells. Due to the nonlinear response in one or more of the subcells, the incremental relations will usually violate the constitutive equations. Thus, an iterative correction scheme is needed to satisfy both the micromechanical constraints and the constitutive equations. The tasks for the micromechanical algorithm can be stated as: Given history variables in the subcells from previous converged solution and a constant average strain rate for the unit cell within the current time increment, update the effective stress, the effective stiffness, and the history variables at the end of the increment.

8.4 The Sublaminar Model

The term *thick-section composite laminate* is herein defined as a multi-layered laminate with a thickness greater than approximately 1/4 in. in which it is possible to identify a repeating sublaminar. The sublaminar consists of the smallest repeating stacking sequence of laminae (Fig. 8.1). Unlike the terminology used in the theory of plates and shells for thick-section structures, the term *thick-section*, used herein, does not always imply the existence of relatively large interlaminar stress and strain distributions. For example, a composite with thickness $t = 1.0$ in., stacking sequence of $[90_2 / 0]_{30S}$, and a radius of curvature of 80 in. and above is not normally considered to be a thick-section in the context of plate or shell theory; however, it does fall under the current definition for thick-section and multilayered composites.

A thick-section composite structure may exhibit nearly linear overall structural behavior almost up to failure. However, nonlinear structural response can also arise locally especially in the presence of edge effects and structural discontinuities, such as crack tips, holes, and cutouts. These stress concentrations can have a significant impact on damage and the overall behavior close to and postultimate. Therefore, it is important to develop analysis methods for thick-section composites that include both 3D and nonlinear capabilities.

In cases where plate or shell structural modeling is appropriate, and where the material response can be considered linear, the cross-sectional stiffness and flexural rigidities can be calculated using the classical laminate theory (CLT). The stress and strain distributions for the individual laminae can be back-calculated from central plane strains and curvatures obtained from the structural analysis. However, the existence of hundreds of individual plies in a typical thick-section composite structure makes ply-by-ply nonlinear analysis impractical. In this case, where nonlinear response and damage and/or interlaminar stress effects are important, the integration of the stress-strain relations must be performed numerically for all plies during the analysis. As a result, the CLT method is very difficult to apply. On the other hand, the large number of repeating plies in thick-section composites produces a structure which is, in effect, much more homogeneous than sections with a small number of plies. This allows for a through-thickness homogenization or “smearing” procedure to be used effectively at the laminate level.

A sublaminar is constructed from the smallest through-thickness repeating stacking sequence. The effective response of the sublaminar is used to define an equivalent nonlinear homogeneous continuum. The

response of a nonlinear response of the composite structure is determined by the effective homogeneous behavior of material points with the few layers of generated by the sublaminates at each integration point in the FE structural mesh.

Figure 8.1 describes a 3D framework for the nonlinear structural analysis of thick-section laminated composites. This general approach involves a material model with a two-level hierarchy: a micromechanical model of a unidirectional lamina and a sublaminates model. The CDC class of micromodels, developed in the previous sections, can be used to represent the nonlinear response of each layer in the sublaminates. The 3D lamination theory is used in a nonlinear formulation to synthesize the effective continuum response of the sublaminates model. The sublaminates material model is designed to function through a standard interface with structural analysis packages; the micromodels and sublaminates model, which constitute a two-level material model, are hidden from element and structural-level processes. The main features of the nonlinear sublaminates model are formulated in this section using the 3D lamination theory to derive thermomechanical effective stress–strain relations for the sublaminates. The instantaneous effective stiffness and thermal coefficients of the sublaminates are then derived.

The 3D lamination theory was used by Pagano [30, 31] to derive the cross-sectional properties of anisotropic laminates. In Pagano's work, the extensional, flexural, and coupling stiffness were generated for the entire section of the laminate. The formulation of Pagano is based on a linear elasticity solution which satisfies the external boundary conditions as well as the interface traction and displacement continuity between the layers. Therefore, the treatment is limited to the case where all force and moment resultants, and surface forces, are spatially constant. Sun and Li [39] employed the same deformation field and derived the extensional effective stiffness properties for a repeating sublaminates. Pecknold [32, 33] presented a simpler approach for deriving the effective properties of anisotropic sublaminates using the same fundamental patterns of deformations. They proposed using a nonlinear micromechanical model for the individual layers in the sublaminates, which is integrated within a 3D FE analysis of thick-section composites. The cross-section is homogenized at a selected number of integration points, and the nonlinear response of the equivalent homogeneous material is obtained using the 3D lamination theory. The key idea is to replace the sublaminates by a well-defined equivalent homogeneous material. The properties of this material are determined by requiring that the two, sublaminates and equivalent continuum, respond identically when subjected to certain fundamental patterns of stress or strain. To satisfy

displacement and traction continuity conditions between the layers, homogeneous in-plane strain and homogeneous out-of-plane stress patterns are used. The conjugate stress and strain components are determined as through-thickness weighted averages of the corresponding quantities in each layer of the sublaminates.

Effective thermoelastic moduli of the sublaminates are derived considering each layer to be a general anisotropic material. The equivalent response of the repeating sublaminates is assumed to represent the average response of a multilayered and thick-section laminate in some local region. In this equivalent continuum approach, certain selected patterns of stress and strain are used to define equivalence between the actual sublaminates and an equivalent homogeneous continuum. This derivation is an exact solution when the applied in-plane strain and the out-of-plane surface tractions are spatially constant. Under these conditions, the interlaminar or out-of-plane stresses are also constant. The field equations in the form of equilibrium, interface traction, and displacement continuity are reviewed next.

It is useful to use the following notations for the stress and strain vectors:

$$\{\sigma\} = \begin{Bmatrix} \sigma_x \\ \sigma_y \\ \tau_{xy} \\ \sigma_z \\ \tau_{xz} \\ \tau_{yz} \end{Bmatrix} \equiv \begin{Bmatrix} \sigma_i \\ \sigma_o \end{Bmatrix}, \quad \{\varepsilon\} = \begin{Bmatrix} \varepsilon_x \\ \varepsilon_y \\ \gamma_{xy} \\ \varepsilon_z \\ \gamma_{xz} \\ \gamma_{yz} \end{Bmatrix} \equiv \begin{Bmatrix} \varepsilon_i \\ \varepsilon_o \end{Bmatrix}. \tag{8.31}$$

In (8.31), all stress and strain vectors are partitioned into in-plane and out-of-plane components. Perfect bond interface conditions are assumed between the layers. Therefore, the displacement continuity conditions at the interfaces are expressed as

$$u_i^{(k)} \left(x_1, x_2, x_3 = \frac{t^{(k)}}{2} \right) = u_i^{(k+1)} \left(x_1, x_2, x_3 = -\frac{t^{(k+1)}}{2} \right), \tag{8.32}$$

where (k) denotes a layer number and is the through-thickness direction. It can be easily verified using (8.32) that the interface displacement continuity equations require that

$$\boldsymbol{\varepsilon}_i^{(k)} \left(x_1, x_2, x_3^{(k)} = \frac{t^{(k)}}{2} \right) = \boldsymbol{\varepsilon}_i^{(k+1)} \left(x_1, x_2, x_3^{(k+1)} = -\frac{t^{(k+1)}}{2} \right). \quad (8.33)$$

The equilibrium and traction continuity at the interface are expressed by:

$$\boldsymbol{\sigma}_o^{(k)} \left(x_1, x_2, x_3^{(k)} = \frac{t^{(k)}}{2} \right) = \boldsymbol{\sigma}_o^{(k+1)} \left(x_1, x_2, x_3^{(k+1)} = -\frac{t^{(k+1)}}{2} \right). \quad (8.34)$$

The interface equations expressed in (8.33) and (8.34), along with the external boundary conditions and the stress–strain relations of the laminae, define the governing field equations.

The effective thermoelastic moduli of the anisotropic sublaminates are defined next. The formulation is expressed in terms of total stress and strain vectors. This formulation also applies in an incremental form for the effective tangent stiffness matrix of the laminate in the case where nonlinear stress–strain response in a layer is considered.

The through-thickness effective stress and strain vectors are defined as

$$\left\{ \begin{array}{c} \bar{\boldsymbol{\varepsilon}} \\ \bar{\boldsymbol{\sigma}} \end{array} \right\} = \frac{1}{t} \sum_{k=1}^N \int_{-t^{(k)}/2}^{t^{(k)}/2} \left\{ \begin{array}{c} \boldsymbol{\varepsilon} \\ \boldsymbol{\sigma} \end{array} \right\}^{(k)} dx_3^{(k)}, \quad (8.35)$$

where t is the sublaminates thickness, $t^{(k)}$ is the k th lamina thickness, and N is the number of laminae in the sublaminates. An upper bar is used to denote a sublaminates effective (global) quantity.

The fundamental patterns of applied stress and strain should include spatially homogeneous patterns to generate the effective response of the multilayered laminate in the form of an equivalent continuum. Examining the previous field equations of the 3D lamination theory, it can be seen that

$\varepsilon_i^{(k)} = \bar{\varepsilon}_i$ and $\sigma_o^{(k)} = \bar{\sigma}_o$ satisfy the interface conditions (8.33) and (8.34), respectively. Therefore, the applied spatially homogeneous patterns are:

$$\left\{ \begin{array}{c} \bar{\varepsilon}_i \\ \text{---} \\ \bar{\sigma}_o \end{array} \right\}. \quad (8.36)$$

Using the interface conditions (8.33) and (8.34), along with the applied homogeneous patterns (8.36), the stress and strain for each lamina (k) are

$$\left\{ \begin{array}{c} \varepsilon_i \\ \text{---} \\ \sigma_o \end{array} \right\}^{(k)} = \left\{ \begin{array}{c} \bar{\varepsilon}_i \\ \text{---} \\ \bar{\sigma}_o \end{array} \right\}, \quad k = 1, \dots, N, \quad (8.37)$$

where (8.37) identically satisfies (8.35). The conjugate effective stresses and strains are expressed, using (8.35), by:

$$\left\{ \begin{array}{c} \bar{\sigma}_i \\ \text{---} \\ \bar{\varepsilon}_o \end{array} \right\} = \sum_{k=1}^N \frac{t^{(k)}}{t} \left\{ \begin{array}{c} \sigma_i \\ \text{---} \\ \varepsilon_o \end{array} \right\}^{(k)}. \quad (8.38)$$

Next, the displacement and traction continuity relations (8.37) are used, along with the stress–strain relations for the laminae, to form the sublaminar effective thermoelastic properties. To this end, the stress–strain relations for each lamina are expressed in the sublaminar global coordinate system. Using the notation of (8.31), the stress–strain relations for lamina (k) are expressed in the global coordinate system as

$$\left\{ \begin{array}{c} \sigma_i \\ \sigma_o \end{array} \right\} = \begin{bmatrix} C_{ii} & C_{io} \\ C_{oi} & C_{oo} \end{bmatrix} \left\{ \begin{array}{c} \varepsilon_i - \Delta T \alpha_i \\ \varepsilon_o - \Delta T \alpha_o \end{array} \right\}, \quad (8.39)$$

where ΔT is the change in temperature and α denotes the thermal expansion coefficients of the lamina. Next, (8.39) is partially inverted to obtain the form

$$\begin{aligned} \begin{Bmatrix} \sigma_i \\ \varepsilon_o - \Delta T \alpha_o \end{Bmatrix} &= \begin{bmatrix} A & B \\ -B^T & D \end{bmatrix} \begin{Bmatrix} \varepsilon_i - \Delta T \alpha_i \\ \sigma_o \end{Bmatrix}, \\ D &= C_{oo}^{-1}, \\ \text{in which } B &= C_{io} C_{oo}^{-1}, \\ A &= C_{ii} - C_{io} C_{oo}^{-1} C_{oi}. \end{aligned} \tag{8.40}$$

Equation (8.40) is merely a general and convenient representation of the stress–strain relations that apply in general to any material with an invertible tangent stiffness matrix. However, this compact representation is an instrumental precursor to the simplified formulation for the effective stiffness of anisotropic laminates. The matrices B and D , defined in (8.40), should not be confused with the coupling and flexural stiffness matrices of the CLT, which are often denoted by the same symbols. Equation (8.40) is further simplified and written as:

$$\begin{Bmatrix} \sigma_i \\ \varepsilon_o \end{Bmatrix} = \begin{bmatrix} A & B \\ -B^T & D \end{bmatrix} \begin{Bmatrix} \varepsilon_i \\ \sigma_o \end{Bmatrix} + \Delta T \begin{bmatrix} -A & 0 \\ B^T & I \end{bmatrix} \begin{Bmatrix} \alpha_i \\ \alpha_o \end{Bmatrix}. \tag{8.41}$$

Substituting (8.37) and (8.41), the stress–strain relation for the k th lamina is:

$$\begin{Bmatrix} \sigma_i \\ \varepsilon_o \end{Bmatrix}^{(k)} = \begin{bmatrix} A & B \\ -B^T & D \end{bmatrix}^{(k)} \begin{Bmatrix} \bar{\varepsilon}_i \\ \bar{\sigma}_o \end{Bmatrix} + \Delta T \begin{bmatrix} -A & 0 \\ B^T & I \end{bmatrix}^{(k)} \begin{Bmatrix} \alpha_i \\ \alpha_o \end{Bmatrix}^{(k)}. \tag{8.42}$$

Equations (8.38) and (8.42) are used to express the effective in-plane stress and out-of-plane strain of the sublaminate as:

$$\begin{Bmatrix} \bar{\sigma}_i \\ \bar{\sigma}_o \end{Bmatrix} = \sum_{k=1}^N \frac{t^{(k)}}{t} \begin{bmatrix} A & B \\ -B^T & D \end{bmatrix}^{(k)} \begin{Bmatrix} \bar{\varepsilon}_i \\ \bar{\sigma}_o \end{Bmatrix} + \Delta T \sum_{k=1}^N \frac{t^{(k)}}{t} \begin{bmatrix} -A & 0 \\ B^T & I \end{bmatrix}^{(k)} \begin{Bmatrix} \alpha_i \\ \alpha_o \end{Bmatrix}^{(k)}. \quad (8.43)$$

It is desired to write the effective stress–strain relations for the sublaminates, similar to the laminae stress–strain relations in (8.39) and (8.41), as:

$$\begin{Bmatrix} \bar{\sigma}_i \\ \bar{\sigma}_o \end{Bmatrix} = \begin{bmatrix} \bar{C}_{ii} & \bar{C}_{io} \\ \bar{C}_{oi} & \bar{C}_{oo} \end{bmatrix}^{(k)} \begin{Bmatrix} \bar{\varepsilon}_i - \Delta T \bar{\alpha}_i \\ \bar{\varepsilon}_o - \Delta T \bar{\alpha}_o \end{Bmatrix}. \quad (8.44)$$

To determine the effective stiffnesses in (8.44), it is first partially inverted in the form

$$\begin{Bmatrix} \bar{\sigma}_i \\ \bar{\varepsilon}_o \end{Bmatrix} = \begin{bmatrix} \bar{A} & \bar{B} \\ -\bar{B}^T & \bar{D} \end{bmatrix} \begin{Bmatrix} \bar{\varepsilon}_i \\ \bar{\sigma}_o \end{Bmatrix} + \Delta T \begin{bmatrix} -\bar{A} & 0 \\ \bar{B}^T & I \end{bmatrix} \begin{Bmatrix} \bar{\alpha}_i \\ \bar{\alpha}_o \end{Bmatrix},$$

$$\bar{D} = \bar{C}_{oo}^{-1}, \quad (8.45)$$

$$\text{where } \bar{B} = \bar{C}_{io} \bar{C}_{oo}^{-1},$$

$$\bar{A} = \bar{C}_{ii} - \bar{C}_{io} \bar{C}_{oo}^{-1} \bar{C}_{oi},$$

and then compared with (8.43) to yield

$$\begin{bmatrix} \bar{A} & \bar{B} \\ -\bar{B}^T & \bar{D} \end{bmatrix} = \sum_{k=1}^N \frac{t^{(k)}}{t} \begin{bmatrix} A & B \\ -B^T & D \end{bmatrix}^{(k)} \quad (8.46)$$

and

$$\begin{bmatrix} -\bar{A} & 0 \\ \bar{B}^T & I \end{bmatrix} \begin{Bmatrix} \bar{\alpha}_i \\ \bar{\alpha}_o \end{Bmatrix} = \sum_{k=1}^N \frac{t^{(k)}}{t} \begin{bmatrix} -A & 0 \\ B^T & I \end{bmatrix}^{(k)} \begin{Bmatrix} \alpha_i \\ \alpha_o \end{Bmatrix}^{(k)}. \quad (8.47)$$

Therefore, the effective tangent stiffness matrix of the sublaminates can be calculated from (8.46) as:

$$\bar{C} = \begin{bmatrix} \bar{C}_{ii} & \bar{C}_{io} \\ \bar{C}_{oi} & \bar{C}_{oo} \end{bmatrix}, \quad \text{where} \quad \begin{aligned} \bar{C}_{oo} &= \bar{D}^{-1}, \\ \bar{C}_{io} &= \bar{B}\bar{D}^{-1}, \\ \bar{C}_{oi} &= \bar{C}_{io}^T, \\ \bar{C}_{ii} &= \bar{A} + \bar{B}\bar{D}^{-1}\bar{B}^T. \end{aligned} \quad (8.48)$$

The effective thermal expansion coefficients of the sublaminates are derived from (8.47) as:

$$\begin{aligned} \bar{\alpha}_i &= \bar{A}^{-1} \sum_{k=1}^N \frac{t^{(k)}}{t} A^{(k)} \alpha_i^{(k)}, \\ \bar{\alpha}_o &= -\bar{B}^T \bar{\alpha}_i + \sum_{k=1}^N \frac{t^{(k)}}{t} \left(B^{(k)T} \alpha_i^{(k)} + \alpha_o^{(k)} \right). \end{aligned} \quad (8.49)$$

8.5 Multiscale Analysis of Thick-Section Pultruded Composites

Thick-section structural components can be manufactured by the pultrusion process using several reinforcement layers with a polymeric resin system. The result is a long prismatic structural component that can have shapes similar to the standard steel shapes, such as wide flange, channels, and angle sections. Layers with continuous filament mat (CFM) reinforcement are heavily used in this process to provide large volume and bind the unidirectional roving layers in transition areas of the prismatic cross-section. The relatively fast production of pultruded structural components allows for mass manufacturing and cost competitive composite materials. Pultruded composites can have a thickness ranging from 1/16 to 1 in. and an overall fiber volume fraction (FVF) of 0.3–0.5.

Due to a relatively low FVF, large thickness, and existence of the polymeric matrix, a nonlinear and time-dependent mechanical response is present. The nonlinear responses coupled with the time-dependent responses affect the overall behavior of the structure. It is important to form a combined material and structural framework that can simultaneously provide effective material and structural analyses.

Several experimental and analytical studies on time-independent buckling and postbuckling of thick-section composite (pultruded) columns have been performed. Vakanier et al. [41] performed linearized buckling analysis of columns with stocky wide-flange (WF) cross-sections using FE models. Most of geometries studied have relatively small slenderness ratio and allow for local flange buckling. Barbero and Tomblin [12] investigated global buckling loads for I-shape long columns. As expected, the results for the long columns were well predicted by the Euler buckling theory. Barbero et al. [10] studied interaction between the local and global buckling modes on intermediate length composite WF columns. Zureick and Scott [42] presented design guidelines for fiber-reinforced polymer (FRP) slender structural members under axial compression load based on global buckling limit states. Axially compression tests on box and I-shape cross-sections of E-glass/vinylester composite specimens were performed. Bank and Yin [8] investigated the postbuckling regime of composite I-beams, focusing on the web-flange junction failure. They performed a FE analysis using a node separation technique to simulate the local separation of the flange from the web following a local buckling of the flange.

Micromechanical modeling approaches in thick-section pultruded composite materials have been studied. Barbero [9, 37] proposed a linear micromechanical modeling approach to generate the overall effective stiffness of thick-section (pultruded) composite material systems. Their micromodel, which employed the periodic microstructure formulae of [11], was combined with the classical lamination theory and mechanics of laminated beams approach to determine the overall effective stiffness of composite beams.

Haj-Ali et al. [16, 19, 20, 22, 23] proposed a multiscale modeling approach for the nonlinear elastic responses of thick-section composite systems with roving and CFM reinforcements. This multiscale framework is schematically illustrated in Fig. 8.3.

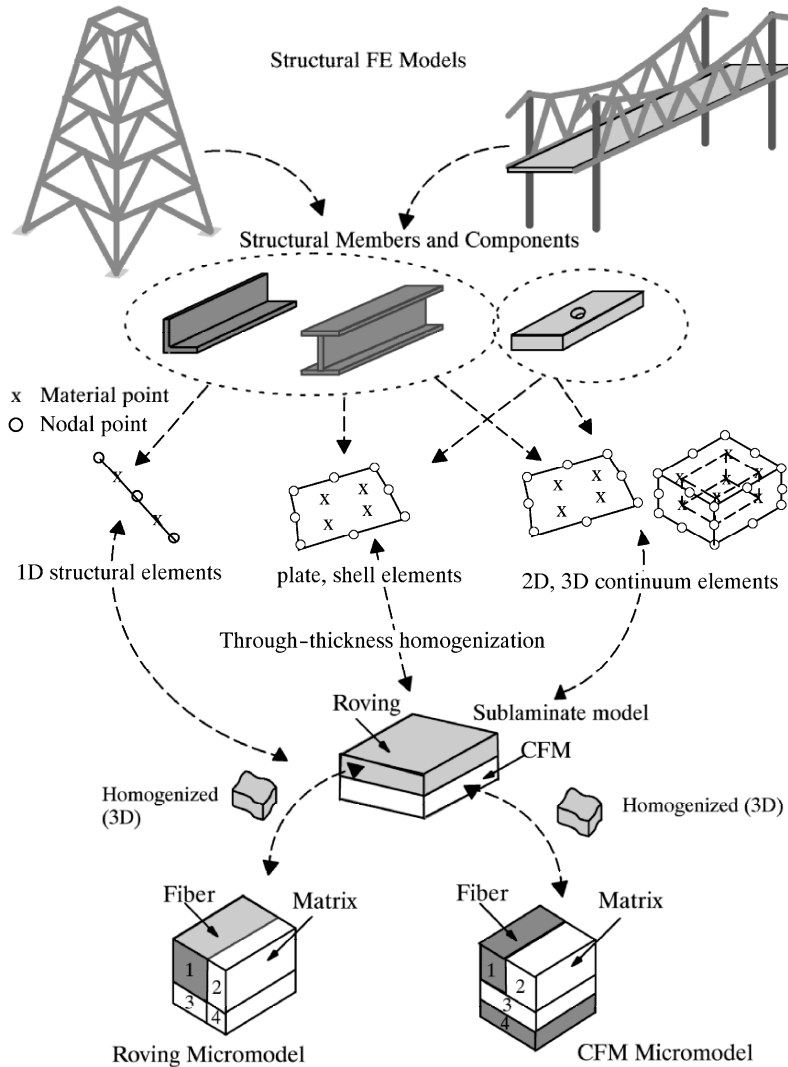


Fig. 8.3. Multiscale structural and micromechanical framework for the analysis of pultruded composite materials and structures (adapted from [21])

Both structural and continuum finite elements can be used. Different micromechanical models are employed for the reinforcement systems in the pultruded layers. Haj-Ali et al. [19, 20] were the first to introduce this combined nonlinear 3D micromechanical modeling approach for pultruded composites. Their framework was time independent and focused mainly on applying continuum elements. The structural level of this framework,

shown in Fig. 8.3, represents FE models for pultruded structures using 1D (beam, truss), 2D (plane, shell), and 3D (brick) elements. A sublaminar model is used at each Gauss point in every element to generate a 3D effective anisotropic nonlinear viscoelastic response of the combined roving and CFM layers. Different stress–strain constraints are imposed on the sublaminar model to properly interface with the 1D, 2D, or 3D elements. In the case where beam and shell elements are used, a uniaxial stress–strain relation and a plane-stress condition must be imposed, respectively. In the lower level, two previously developed 3D micromechanical material models are then used for the roving and CFM layers [20, 21, 23].

Deformation plasticity with a Ramberg–Osgood strain–stress curve was used to describe the nonlinear static response in the matrix system. Tension and compression tests on off-axis coupons made of E-glass fiber and vinylester matrix were conducted to calibrate linear and nonlinear elastic material properties and to validate their proposed modeling approach. It was shown that the nonlinearity in the material response is significant for the off-axis specimens even for relatively low load levels. Haj-Ali and Muliana [21, 23] proposed a new *nonlinear* and *time-dependent* formulation for multilayered composite systems. The Schapery constitutive model [22, 35] was used for the time-dependent behavior of the isotropic matrix. Short-term off-axis creep compression tests on E-glass/vinylester coupons were performed to calibrate the nonlinear time-dependent material properties and to verify their proposed micromodels. Haj-Ali and Muliana [22] performed an integrated micromechanical–structural modeling approach to analyze creep behaviors of composite structures. The previously developed time-dependent micromechanical models of roving and CFM were used within continuum typed elements in general FE analyses. Creep responses of notched plate composite plates were used to validate the integrated micromechanical–structural modeling approach.

Studies on long-term behaviors of thick-section layered FRP composites are limited. Several experimental and analytical works have been focused on the uniaxial viscoelastic responses on composite specimens and structural components [7, 27, 28, 36, 38]. Spence [38] performed tests on unidirectional glass/epoxy pultruded coupons under compression creep for 840 h. The creep response was pronounced for applied loads higher than 30% of the compressive strength. Bank and Mosallam [7] conducted long-term creep tests for E-glass/vinylester structural members with continuous strand mat and roving layers. A plane portal frame, 6 ft. high \times 9 ft. wide, was tested under a load level of 25% of the ultimate failure for 10,000 h.

Scott and Zureick [36] conducted compression creep tests on pultruded E-glass/vinylester coupons cut from I-shape pultruded sections in their longitudinal direction. The samples were subjected to three different stress levels for the duration, up to 16 months. Findley power law model was used with a constant exponent to calibrate their uniaxial time-dependent behavior. The stress-dependent coefficients were calibrated from the short duration tests (1,000 h).

Long-term behavior, such as creep buckling of thick-section composites, has not been widely addressed, especially using a multiscale modeling approach. This study presents a multiscale nonlinear viscoelastic framework for the time-dependent behavior of composite materials and structural systems. The multiscale modeling approach is a local–global structural framework that can integrate different constitutive material models at the lowest material scales, namely the fiber and polymeric matrix constituents. It can also generate the effective nonlinear anisotropic continuum response that is needed at the structural level. The composite system studied is reinforced with roving and CFM layers. The constitutive characterization for the fiber and matrix constituents is performed at the lowest level of the multiscale modeling framework. The Schapery's nonlinear single integral model is applied for the polymeric matrix system. It is assumed that both matrix constituents in the roving and CFM unit cells have the same isotropic nonlinear viscoelastic properties. An overall

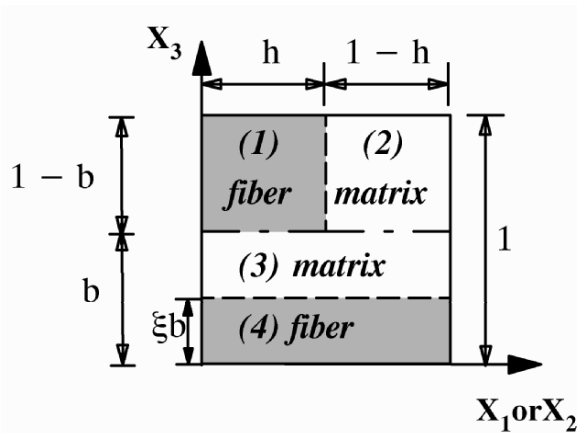


Fig. 8.4. Unit cell for the CFM layers in a pultruded composite

$$\bar{D}^T = \left[\begin{array}{c|c|c|c|c|c|c|c|c} \mathbf{I} & \mathbf{I} & \frac{V_1+V_2}{V_1} \mathbf{I} & \mathbf{0} & \mathbf{0} & \mathbf{0} & \mathbf{0} & \mathbf{0} \\ \hline (3 \times 3) & (3 \times 3) \\ \hline \mathbf{0} & \mathbf{0} & \mathbf{0} & \frac{V}{V_1} \mathbf{I} & \mathbf{0} & \mathbf{0} & \mathbf{0} & \mathbf{0} \\ \hline (3 \times 3) & (3 \times 3) \end{array} \right] \quad (8.55)$$

where the variable V_α indicates unit volume fraction of the subcell number α .

The linearized micromechanical relations, derived in incremental formulation, will usually violate the constitutive equations because of the nonlinear and time-dependent response in the matrix subcells. An iterative correction scheme is needed to satisfy both the micromechanical constraints and the constitutive equations. The linearized micromechanical relations with tangential material matrices are used to generate trial incremental stresses and strains for the subcells (trial solution). The total micromechanical relations are then used to define a residual error for each micromodel. This residual is then used to correct the trial solution. This process is repeated until a converged solution that satisfies both micromechanical and nonlinear equations is reached.

A correction algorithm is needed in every nested micromodel. The input is in the form of an applied incremental strain. The stress–strain states from the previous step and the history variables are the known variables for each nested micromodel and scale. Inside the sublaminar model, the strain increment is distributed to the roving and CFM micromodels. Iterative correction schemes are developed separately for the roving and CFM models to minimize the errors and satisfy the micromechanical and constitutive relations. At the roving and CFM systems, the current stress–strain states, the tangent stiffness, together with the history variables are updated and sent to the sublaminar level. An iterative procedure is also performed inside the sublaminar system until the actual stress–strain relations, as well as homogenization constraints, are satisfied. Any iteration at the sublaminar level requires the full calculation procedure from the lower levels of the framework. Once all levels of error are satisfied, the sublaminar effective nonlinear continuum state is defined and communicated to the FE structural level.

8.6 Applications

Haj-Ali and Muliana [22, 23] examined the ability of the multiscale formulation to predict the nonlinear viscoelastic behavior of composite materials and structures. The effective response is generated from calibrated in situ properties of the matrix and fiber constituents. To that end, different creep tests available in the literature are used. Off-axis test results are available for glass/epoxy [26] and T300/5208 graphite/epoxy [40] composites. Prediction of the calibrated model is examined against test results not used in the calibration process. The current approach is similar but employs a refined 3D micromodel that can ultimately be used in both 2D and 3D structural models. Creep test results on glass/epoxy off-axis composite specimens reported by Lou and Schapery were used for validation of the current modeling approach. Linear viscoelastic calibration was performed using results from the 45° off-axis specimen under the lowest applied axial stress (1.382 ksi). Overall, the nonlinear calibration strikes a balance between all nonlinear curves as seen in Figs. 8.5 and 8.6.

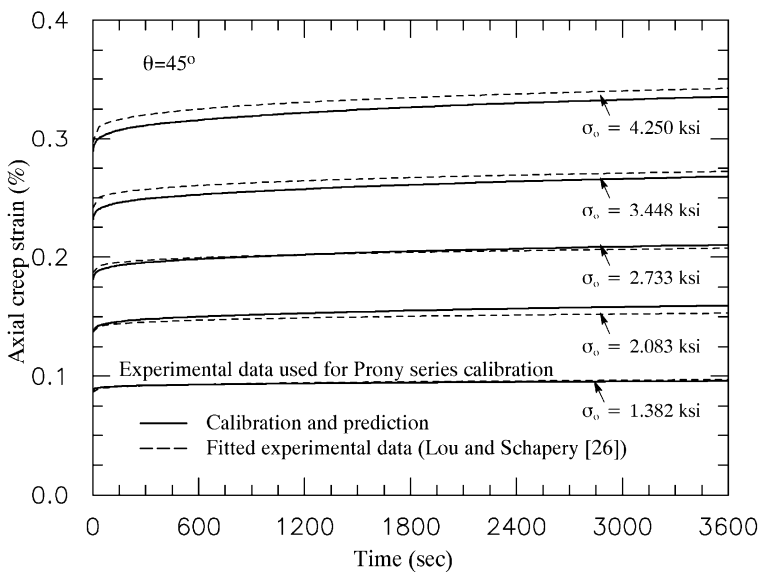


Fig. 8.5. Axial creep strain for 45° off-axis glass-epoxy laminate (adapted from [23])

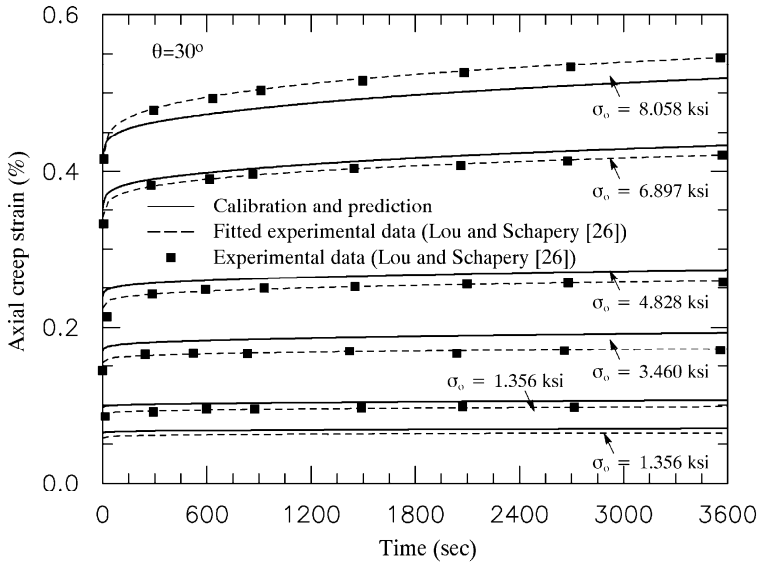


Fig. 8.6. Axial creep strain for 30° off-axis glass-epoxy laminate (adapted from [23])

Haj-Ali and Kilic [19, 20] applied the multiscale nonlinear models to predict the nonlinear response of thick-section pultruded plates under multiaxial stress–strain states. To this end, a series of tests were performed with off-axis notched pultruded plates subject to uniaxial compression. Four uniaxial strain gages were attached on the back and front surfaces of each plate. The off-axis angles used in the notched plates were 0°, 15°, 30°, 45°, 60°, and 90°. The multiscale framework was implemented in the [1] general FE code.

Figure 8.7 shows the off-axis tests and FE results in the form of the fourth strain gage (G4) that is the closest to the edge of the hole. A consistent softer response is shown from the G4 curves for all off-axis tests. As expected, the level of nonlinear response varies from the different plates, increasing with the increased off-axis angle. Compression buckling was monitored by examining the difference in the back-to-back strains. It was concluded that no significant out-of-plane bending occurred in these tests prior to reaching their ultimate loading states. Overall, very good prediction is shown by the FE models compared with the experimental results. This confirms the ability of the micromodels to predict a nonlinear multiaxial state of deformation with stress concentration due to the notched holes.

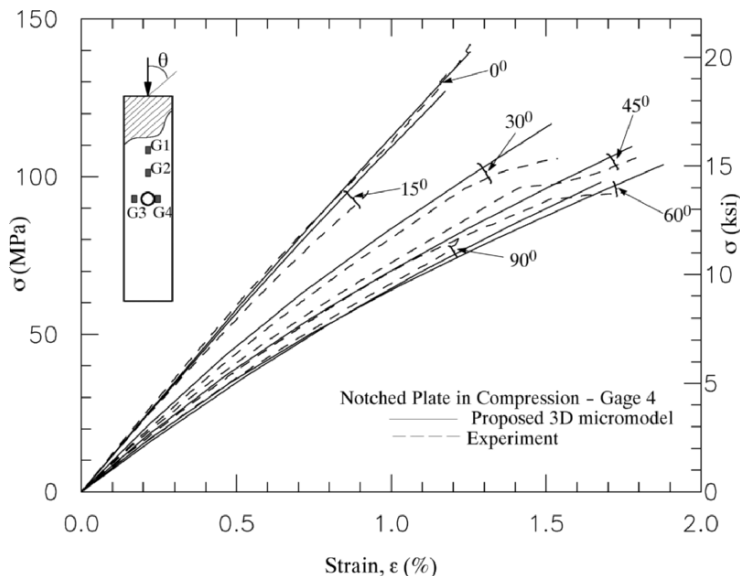


Fig. 8.7. Experimental and FE remote compression stress vs. axial strain measured from G4 for different off-axis orientations of notched pultruded composite plate (adapted from [20])

A nested 3D micromechanical and structural framework is presented for the nonlinear elastic, viscoelastic, and crack growth analysis of thick-section and multilayered composite materials. Micromodels for a unidirectional lamina, an in-plane random medium phenomenological model, and a sublaminar model for effective continuum response of a through-thickness repeating stacking sequence are formulated and integrated in the material–structural modeling approach. Numerical predictor–corrector stress-update algorithms are used and nested in all hierarchies. The analysis framework is general and can be used with a displacement-based nonlinear FE code. It can incorporate time, temperature, and moisture effects. Several structural simulations are demonstrated to illustrate the effectiveness of the framework.

Haj-Ali and El-Hajjar [13–15, 17, 18] performed experimental and numerical analyses to determine the translayer Mode I and Mode II fracture toughness and crack growth of a thick-section FRP pultruded composite using the proposed multiscale material and structural framework.

Crack growth tests with crack tip opening displacement (CTOD) measurements were conducted for different crack length to width ratios (a/W) as shown in Fig. 8.8. Figure 8.9 shows that the computational cohesive models were calibrated and used to predict Mode I and Mode II crack growth for eccentrically loaded single-edge-notch (tension), ESE(T), and notched butterfly specimens using a modified Arcan fixture. Figure 8.10 illustrates the predicted capability of the combined cohesive FE modeling with the proposed multiscale constitutive framework compared to experimental results in the form of load vs. CTOD and in the form of crack length vs. CTOD. The validity of the multiscale modeling approach before the onset of crack growth was also investigated using a new infrared thermography (IR) method [13–15]. The multiscale constitutive framework, combined with cohesive models, was shown to be effective in predicting the failure load and crack growth behavior in thick-section composites.

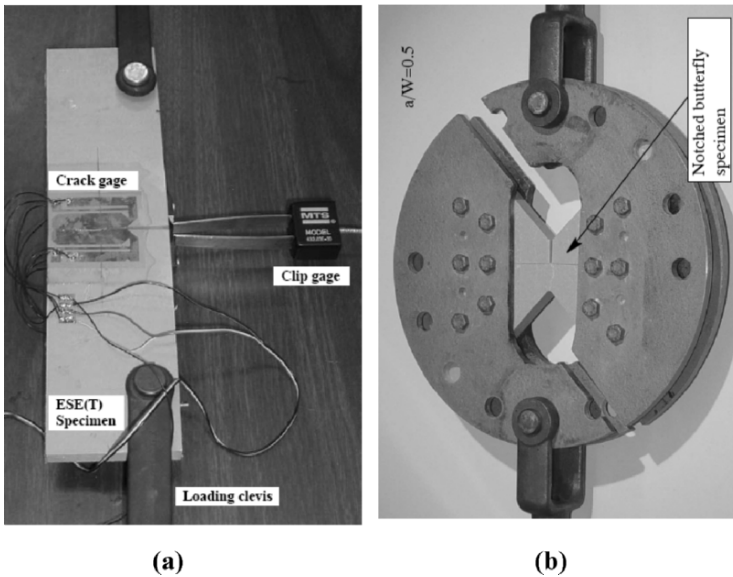


Fig. 8.8. Two test setups: (a) fracture test with crack monitoring gage bonded to ESE(T) specimen and (b) modified Arcan fixture used for Mode II fracture testing (adapted from [18])

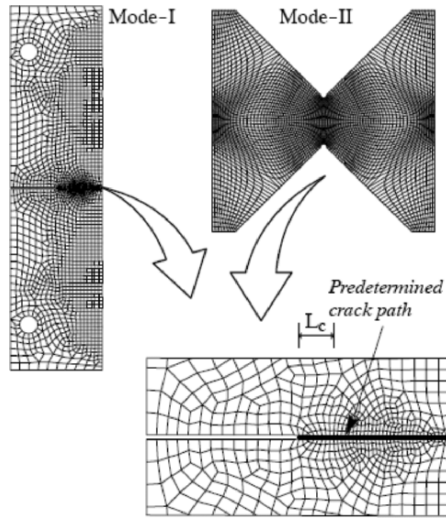


Fig. 8.9. Cohesive fracture modeling of through-crack in thick-section composites using FE cohesive models along with the multiscale material and structural modeling framework (adapted from [18])

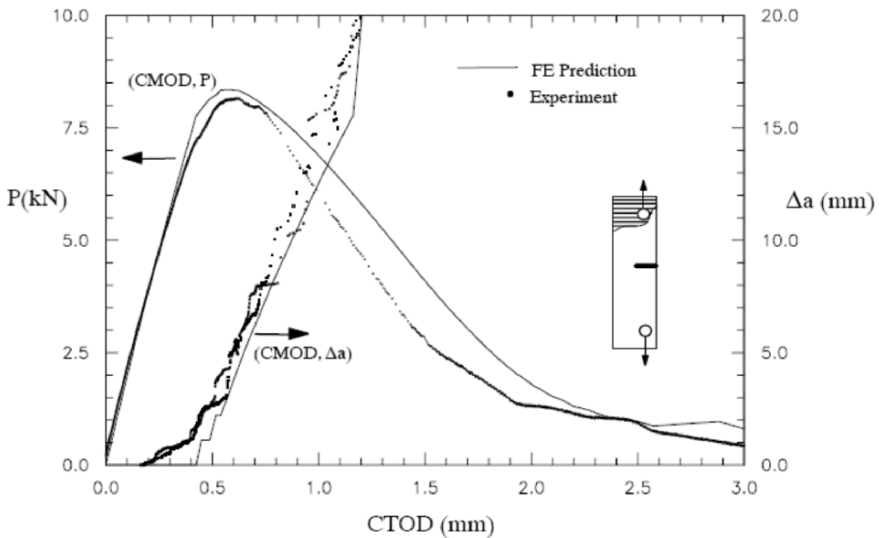


Fig. 8.10. Predicted crack growth for transversely oriented reinforcement of an ESE(T) composite specimen with $a/W=0.3$ using cohesive FE model with the multiscale material framework (adapted from [18])

8.7 Conclusions

Effective multiscale micromechanical and structural frameworks are formulated for the nonlinear analysis of multilayered and thick-section FRP composite materials. The micromechanical models explicitly recognize the response of the layered composite systems and their fiber–matrix constituents. A unified numerical formulation is presented for a class of simplified micromodels. The formulation allows efficient application of the micromodels in large-scale nonlinear FE analysis of composite structures, where very large numbers of micromechanical calculations are carried out. Therefore, it is crucial that the proposed nonlinear stress-update and stress-correction algorithms are efficient and robust. The proposed material and structural framework were shown to be effective in predicting the nonlinear and time-dependent responses of laminated and pultruded FRP composites.

Acknowledgments

The author wishes to acknowledge past and continued support by the National Science Foundation (NSF) through the Civil and Mechanical Systems (CMS) Division under grant numbers 0409514 and 9876080. Previous partial grants from Lockheed Martin Co. under the Composites Affordability Initiative are also appreciated.

References

1. ABAQUS, Hibbitt, Karlsson, and Sorensen, Inc., User's Manual, Version 6.3 (2006)
2. Aboudi J (1987) Closed form constitutive equations for metal matrix composites. *Int. J. Eng. Sci.*, 25, 1229
3. Aboudi J (1989) Micromechanical analysis of composites by the method of cells. *Appl. Mech. Rev.*, 42(7), 193–221
4. Aboudi J (1990) The nonlinear behavior of unidirectional and laminated composites – a micromechanical approach. *J. Reinf. Plast. Compos.* 9, 13–32
5. Aboudi J (1991) *Mechanics of Composite Materials – A Unified Micromechanical Approach*. Elsevier, New York
6. Aboudi J (1993) Constitutive behavior of multiphase metal matrix composites with interfacial damage by the generalized cells model. In: *Damage in Composite Materials*, ed. Voyiadjis GZ, Elsevier, New York

7. Bank LC and Mosallam AS (1990) Creep and failure of a fill-size fiber reinforced plastic pultruded frame. *ASME Petrol. Div. Pub.: Compos. Mater. Technol.*, 32, 49–56
8. Bank LC and Yin J (1999) Failure of web-flange junction in postbuckled pultruded i-beams. *J. Compos. Constr.*, 3(4), 177–184
9. Barbero EJ (1991) Pultruded structural shape – from the constituents to the structural behavior. *SAMPE J.*, 27(1), 25–30
10. Barbero EJ, Dede EK, and Jones S (2000) Experimental verification of buckling-mode interaction in intermediate-length composite columns. *Int. J. Solids Struct.*, 37(29), 3919–3934
11. Barbero EJ and Luciano R (1995) Micromechanical formulas for the relaxation tensor of linear viscoelastic composites with transversely isotropic fibers. *Int. J. Solids Struct.*, 32(13), 1859–1872
12. Barbero EJ and Tomblin J (1993) Euler buckling of thin-walled composite columns. *Thin-Walled Struct.*, 17(4), 237–258
13. El-Hajjar RF and Haj-Ali RM (2003) A quantitative thermoelastic stress analysis method for pultruded composites. *Compos. Sci. Technol. J.*, 63(7), 967–978
14. El-Hajjar RF and Haj-Ali RM (2004) In-plane shear testing of thick-section pultruded frp composites using a modified arcan fixture. *Compos. Part B: Eng.*, 35(5), 421–428
15. El-Hajjar RF and Haj-Ali RM (2004) Infrared (IR) thermography for strain analysis in fiber reinforced plastics. *Exp. Tech.: Soc. Exp. Mech.*, 28(2), 19–22
16. El-Hajjar RF and Haj-Ali RM (2005) Mode-I fracture toughness testing of thick section frp composites using the ese(t) specimen. *Eng. Fract. Mech.*, 72(4), 631–643
17. Haj-Ali RM and El-Hajjar RF (2003) Crack propagation analysis of mode-i fracture in pultruded composites using micromechanical constitutive models. *Mech. Mater.*, 35(9), 885–902
18. Haj-Ali RM, El-Hajjar RF, and Muliana HA (2006) Cohesive fracture modeling in thick-section composites. *Eng. Fract. Mech.* (in press)
19. Haj-Ali RM and Kilic MH (2002) Nonlinear behavior of pultruded FRP composites. *Compos. Part B: Eng.*, 33(3), 173
20. Haj-Ali RM, Kilic MH, and Zureick AH (2001) Three-dimensional micromechanics based constitutive framework for analysis of pultruded composite structures. *ASCE J. Eng. Mech.*, 127(7), 653–660
21. Haj-Ali RM and Muliana AH (2003) Micromechanical constitutive framework for the nonlinear viscoelastic behavior of pultruded composite materials. *Int. J. Solids Struct.*, 40(5), 1037–1057
22. Haj-Ali RM and Muliana AH (2004) Numerical finite element formulation of the Schapery nonlinear viscoelastic material model. *Int. J. Numer. Meth. Eng.*, 59(1), 25–45
23. Haj-Ali RM and Muliana AH (2004) A multiscale constitutive framework for the nonlinear analysis of laminated composite materials and structures. *Int. J. Solids Struct.*, 41(13), 3461–3490

24. Haj-Ali RM and Pecknold DA (1996) Hierarchical material models with microstructure for nonlinear analysis of progressive damage in laminated composite structures. Structural Research Series No. 611, UILU-ENG-96-2007, Department of Civil Engineering, University of Illinois at Urbana-Champaign
25. Haj-Ali RM, Pecknold DA, and Ahmad MF (1993) Combined micro-mechanical and structural finite element analysis of laminated composites. ABAQUS Users' Conference, Aachen, Germany, pp 233–247
26. Lou YC and Schapery RA (1971) Viscoelastic characterization of a nonlinear fiber-reinforced plastic. *J. Compos. Mater.*, 5, 208–234
27. McClure G and Mohammadi Y (1995) Compression creep of pultruded e-glass reinforced plastic angles. *J. Mater. Civil Eng.*, 7(4), 269–276
28. Mottram JT (1993) Short and long-term structural properties of pultruded beam assemblies fabricated using adhesive bonding. *Compos. Struct.*, 25(1–4), 387–395
29. Muliana AH and Haj-Ali RM (2004) Nested nonlinear viscoelastic and micromechanical models for the analysis of pultruded composite materials and structures. *Mech. Mater.*, 36(11), 1087–1110
30. Pagano NJ (1971) Stress gradients in laminated composite cylinders. *J. Compos. Mater.*, 5, 260–265
31. Pagano NJ (1974) Exact moduli of anisotropic laminates. In: *Mechanics of Composite Materials*, ed. Sendeckyj GP, Academic, New York, pp 23–44
32. Pecknold DA (1990) A framework for 3-d nonlinear modeling of thick-section composites. DTRC-SME-90/92, David Taylor Research Center, Bethesda, MD
33. Pecknold DA and Haj-Ali RM (1993) Integrated micromechanical/structural analysis of laminated composites. In: *Mechanics of Composite Materials – Nonlinear Effects*, ed. Hyer MW, SES/ASME/ASCE Joint meeting, Charlottesville, VA, AMD, Vol. 159, pp 197–206
34. Pecknold DA and Rahman S (1994) Micromechanics-based structural analysis of thick laminated composites. *Comput. Struct.*, 51(2), 163–179
35. Schapery RA (1969) On the characterization of nonlinear viscoelastic materials. *Polym. Eng. Sci.*, 9(4), 295
36. Scott DW and Zureick AH (1998) Compression creep of a pultruded e-glass/vinylester composite. *Compos. Sci. Technol.*, 58(8), 1361–1369
37. Sonti SS and Barbero E (1996) Material characterization of pultruded laminates and shapes. *J. Reinf. Plast. Compos.*, 15(7), 701–717
38. Spence BR (1990) Compressive viscoelastic effects (creep) of a unidirectional glass/epoxy composite material. *Proceedings of 35th International SAMPE Symposium*, April 2–5, Vol. 35(2), pp 1490–1493
39. Sun CT and Li S (1988) Three-dimensional effective elastic constants for thick laminates. *J. Compos. Mater.*, 22, 629–639
40. Tuttle ME and Brinson HF (1986) Prediction of the long-term creep compliance of general composite laminates. *Exp. Mech.*, 26, 89–102

41. Vakanier AR, Zureick A, and Will KM (1991) Predictions of local flange buckling in pultruded shapes by finite element analysis. In: Proceedings of the ASCE Specialty Conference on Advanced Composite Materials in Civil Engineering and Structure, ASCE Material Engineering Division, eds. Iyer SL and Sen R, New York, pp 302–312
42. Zureick A and Scott D (1997) Short-term behavior and design of fiber reinforced polymeric slender members under axial compression. *J. Compos. Constr.*, ASCE, 1(1), 140–149